Journal of
Materials Chemistry A

The effects of aluminum concentration on the microstructural and electrochemical properties of lithium lanthanum zirconium oxide

Journal:	*Journal of Materials Chemistry A*
Manuscript ID	TA-ART-05-2022-003676.R1
Article Type:	Paper
Date Submitted by the Author:	04-Aug-2022
Complete List of Authors:	Moy, Alexandra; University of Michigan, Department of Materials Science and Engineering Häuschen, Grit; Forschungszentrum Jülich GmbH, Institute of Energy and Climate Research Fattakhova-Rohlfing, Dina; Forschungszentrum Jülich GmbH, Institute of Energy and Climate Research Wolfenstine, Jeffrey; Solid Ionic Consulting Finsterbusch, Martin; Forschungszentrum Jülich GmbH, Institute of Energy and Climate Research Sakamoto, Jeffrey ; University of Michigan, Department of Mechanical Engineering

The effects of aluminum concentration on the microstructural and electrochemical properties of lithium lanthanum zirconium oxide

Alexandra C. Moy[1], Grit Häuschen[3], Dina Fattakhova-Rohlfing[3], Jeffrey B. Wolfenstine[4], Martin Finsterbusch[3], and Jeff Sakamoto[1,2,*]

Footnotes

1 Department of Materials Science and Engineering, University of Michigan, Ann Arbor, MI, USA 48109

2 Department of Mechanical Engineering, University of Michigan, Ann Arbor, MI, USA 48109

3 Forschungszentrum Jülich GmbH, Institute of Energy and Climate Research, IEK-1 Jülich, Germany 52428

4 Solid Ionic Consulting, Seattle, WA, USA 98115

*Corresponding author (jeffsaka@umich.edu)

An electronic supplemental information file is available.

Abstract

Cubic lithium lanthanum zirconium oxide ($Li_{7-x}Al_xLa_3Zr_2O_{12}$, LLZO) garnet has gained attention as a promising next-generation electrolyte for lithium batteries due to its high ionic conductivity and chemical stability with lithium metal. The high conductivity can be achieved through doping over a range of aluminum concentrations. In this study, we hot-pressed samples to achieve <2% nominal porosity with aluminum concentrations from $x=0.25$-0.55 mol to understand the effect of aluminum on microstructure and electrochemistry. It was observed that beyond the aluminum solubility limit ($x=\sim0.40$), resistive secondary phases formed at the grain boundaries. As a result, the percent grain boundary resistance increased from 17.6 to 41.2% for $x=0.25$ and $x=0.55$, respectively. Both the grain boundary and bulk activation energies remained relatively constant as the aluminum concentrations increased (~0.44 eV and ~0.39 eV, respectively). It was, therefore, surmised that the mobility term of the Nernst-Einstein equation was roughly independent of aluminum concentration and the major variable controlling bulk conductivity was the number of lithium charge carriers. As a result, as the aluminum concentration increased from $x=0.25$ to $x=0.55$ the bulk conductivity decreased from 0.56 to 0.15 mS/cm. Following these trends of increasing grain boundary resistance and decreasing bulk conductivity with increasing aluminum concentration, $x=0.25$ had the highest total conductivity (0.46 mS/cm). We demonstrated that aluminum concentration has a significant effect on the microstructure and electrochemical properties of LLZO. We believe this work could help understand how to link processing, microstructure, and electrochemical properties to guide the manufacturing of LLZO for use in solid-state batteries.

1. Introduction

Increases in the energy density of lithium-ion batteries are necessary to achieve the goals of next generation applications, such as long range electric vehicle operation.[1–6] Lithium anode technologies offer significant promises in increasing this energy density.[4–9] Use of the lithium anode allows for access to energy densities dramatically higher compared to batteries using the state-of-the-art graphite anode (3860 mAh/g vs. 372 mAh/g).[7–11] However, it is generally known that it is challenging to cycle lithium metal anodes with liquid electrolytes due to dendrite formation.[4,5,7,8] Compared to liquid electrolytes, solid electrolytes are intrinsically safe and thus have the potential to enable lithium metal anodes and, thus, high energy density batteries.[8,9,12–15]

Due to its relatively high ionic conductivity (~1 mS/cm), chemical stability against lithium metal, and its wide electrochemical window, cubic garnet-structured lithium lanthanum zirconium oxide (LLZO), with nominal composition $Li_7La_3Zr_2O_{12}$, has shown significant potential as a next generation electrolyte compared to other solid electrolytes.[1,16,17] LLZO can exhibit two polymorphs, the tetragonal and the cubic.[18–21] The high temperature cubic phase has lithium-ion conductivity two orders of magnitude higher than the tetragonal phase.[18,20,22–25] Stabilization of the cubic over the tetragonal phase at room temperature is commonly achieved through the addition of dopants such as tantalum, aluminum, and gallium, among others.[1,19,21,24,26–36] However, due to its low cost, relative abundance, and low toxicity, aluminum is one of the most industrially attractive choices.

Unfortunately, a comprehensive investigation of aluminum as a dopant and its effect on the crystallographic phase, microstructure, and resulting electrochemical performance is still missing. Given the high interest in LLZO and popularity of aluminum as a dopant, it is especially important to understand the effective concentration of aluminum. With respect to stabilizing the cubic phase, Rangasamy, *et. al.* previously found that cubic phase stability was reached within 0.204-0.352 mol (0.65-1.12 wt.%) of aluminum without excess lithium.[21] Similarly, Düvel, *et. al.*

found cubic phase stability between 0.20-0.40 mol (0.64-1.28 wt.%) of aluminum in LLZO synthesized without excess lithium.[37] When 9.62 wt.% excess lithium was added, they found cubic phase stability as high as 0.60 mol (1.92 wt.%) of aluminum.[37] Sudo, *et. al.* also found a similar range of cubic phase stability, 0.6-1.18 wt.% aluminum, but with 10% excess lithium.[38] In contrast, Jin and McGinn studied a range of 0-2.5 wt.% aluminum with 10% excess lithium and only found cubic phase stability at 1.2 wt.% aluminum.[36] The source of the varying phase stability ranges with respect to aluminum concentration between the studies has not yet been determined and, thus, highlights a need to further investigate where variations could be arising.

The microstructure of the samples reported in literature is varying and often poorly reproducible, since the impact of aluminum concentration on sintering is not well understood. It has been suggested that lithium aluminates form at the grain boundaries and act as sintering aids and grain growth aids.[19,36,39–42] Work by Jin and McGinn and Wolfenstine, *et. al.* suggest that at and above the eutectic point of the Li_2O and Al_2O_3 phase diagram (1055^oC) liquid phase sintering may occur.[36,39,43] Their work suggests that if aluminum doping acts as a sintering aid below this temperature it may only increase diffusion in the grains or occur only above a threshold aluminum concentration. Besides these works there is no other known experimental evidence to support the formation of lithium aluminates or their role as a sintering aid. As such, it would be beneficial to further investigate this phenomenon to increase the understanding of the effect of aluminum doping on sintering and its resulting role in phase purity and microstructure.

In addition to its effect on phase stability and microstructure, aluminum will affect the electrochemical performance of cubic LLZO.[36,38,44] There are a few theoretical studies on the role of aluminum and lithium site occupancy on LLZO conductivity, though results regarding the overall effect of aluminum concentration on bulk lithium-ion conductivity are not conclusive.[42,44,45] Only a few results from experimental studies are available and were mainly obtained by pressure-less sintering, leading to large variation in microstructure and phase content.[36,38,46] Smetaczek, *et. al.* found no correlation between aluminum concentration and conductivity.[46] In contrast, Sudo, *et. al.* observed a clear trend with increasing aluminum concentration.[38] They found a decrease in total, grain, and grain boundary conductivity.[38] Jin and McGinn also noted a decrease in conductivity once cubic phase stability was reached.[36] However, they observed the cubic phase at only two aluminum concentrations (1.2 wt.% and 2.5 wt.% aluminum), and the highest concentrations of secondary phases were present at the highest doping level.[36] The observed variation in conductivity data and the limited amount of previous work highlight the significant knowledge gaps that need to be addressed to understand how best to synthesize LLZO to achieve optimized bulk conductivity.

From these examples, it is clear that the focus of the previous studies on the variation of aluminum concentration has largely been on the effects on a single property, such as phase purity[21,37] or electrochemical behavior[44,46]. However, there are few papers that simultaneously reported on phase purity, electrochemical behavior, and sintering as a function of aluminum concentration and linked their effects together.[36,38] To link these properties while minimizing effects of unintentional variations in composition and microstructure, hot-pressing was used to process the samples. Hot-pressing allows samples to be produced with high density and minimal lithium-loss, resulting in a decrease in secondary phase formation.[21] This method also avoids the aluminum contamination common in pressure-less sintering methods.[21] Hot-pressing, therefore, allowed for less variability and better comparison between compositions compared to pressure-less sintering methods. In this paper, we aim to fill in the gaps of these previous works by using hot-pressing and a unique suite of characterization methods. These methods provide a deeper understanding of the effects of aluminum on the phase purity window, microstructure, and electrochemical properties, such as total and bulk conductivity, grain boundary resistance, and activation energy for bulk and grain boundary lithium transport in LLZO.

To understand the linked effects of aluminum concentration variation on the phase purity, microstructure, and electrochemical behavior of LLZO, $Li_{7-3x}Al_xLa_3Zr_2O_{12}$ powders were synthesized where x varied between 0.25 and 0.55. These powders were then densified via rapid induction hot-pressing. The phase purity, microstructure, and grain boundary characteristics as a function of aluminum concentration were characterized via X-ray diffraction, scanning electron microscopy, electron backscatter diffraction, energy dispersive X-ray spectroscopy, and time-of-flight secondary ion mass spectrometry. Electrochemical properties (bulk conductivity and grain boundary resistance and their representative activation energy for lithium transport) as a function of aluminum concentration were characterized via electrochemical impedance spectroscopy. Ultimately, the investigation of aluminum doping, processing, and microstructure and their effects on electrochemical performance can further improve our understanding of how to design the solid electrolyte for its application in solid-state batteries.

2. Experimental

2.1. Powder synthesis, pellet processing of the solid-state electrolyte, electron backscatter diffraction, and electron dispersive X-ray analysis

$Li_{7-3x}Al_xLa_3Zr_2O_{12}$ was synthesized via solid state reaction with x set to 0.25, 0.35, 0.45, or 0.55. These compositions will be referred to as LLZO-Al0.25, LLZO-Al0.35, LLZO-Al0.45, and LLZO-Al0.55, respectively. This range was selected as 0.25 mol of aluminum appeared to approach the minimum concentration required for cubic phase stability while 0.55 mol of aluminum allowed for observation of samples beyond the aluminum solubility limit.[21,36–38] Intervals of 0.1 mol aluminum were chosen so compositions would remain distinct even within reasonable error in the compositional make-up. The powders were prepared using a 3-step calcination approach, details of which can be found in numerous previous publications, especially for aluminum only substituted LLZO.[47,48] As detailed in previous publications, powders are calcined for 20 hours at 850°C and then twice for 10 hours at 1000°C.[48] However, in contrast to the synthesis of powder for pressure-less sintering reported earlier, the compositions were adapted to the specific need of hot-pressing. Since LLZO-Al0.25 and LLZO-Al0.35 showed neglectable lithium loss during calcination, no excess lithium was added before calcination (Figure S1). For LLZO-Al0.45 and LLZO-Al0.55, some lithium loss was observed which required a 10 mol% lithium-excess for compensation (Figure S1). Compositional make-ups of the powders were confirmed via inductively coupled plasma spectroscopy (ICP-OES) using an iCAP 7600 (Thermo Fisher Scientific) (Table S1). The powders were dissolved using the hot plate-digestion method, details can be found in our earlier work.[49]

The powders of each composition were hot-pressed at 47 MPa and 1225°C for 40 minutes using rapid induction hot-pressing (RIHP) in a flowing argon atmosphere. The presence of pressure allowed for a decrease in sintering time at comparable temperatures to traditional sintering methods, decreasing the likelihood of lithium loss.[22,23,47,48] After hot-pressing, each billet was cut into pellets (~1.1 mm thick) using a diamond saw. The pellets were cut to achieve parallel faces by grinding with 400 grit sandpaper and a lapping fixture (PELCO 15000 micrometer-controlled lapping fixture, Ted Pella) and then manually ground using 600 grit and 1200 grit sandpaper. The pellets were then polished using 15 μm, 6 μm, 1 μm, 0.5 μm, and 0.1 μm diamond polishing compounds with a glycol-based diamond extender (EcoMET 300 Pro, Buehler). For each polishing step, 10 N of force was applied to each pellet and the head and base were rotated at 210 rpm and 60 rpm, respectively. For electron backscatter diffraction (EBSD) analysis and electron dispersive X-ray analysis (EDS), an additional polishing step was performed with 0.03 μm colloidal silica suspension on a felt pad using a lapping fixture (PELCO 15000 micrometer-controlled lapping fixture, Ted Pella). EBSD and EDS measurements were conducted using an EBSD and EDS detector and TEAM software on a Tescan MIRA3 FEGSEM. The collected EBSD and EDS data were analyzed using EDS OIM data collection software. The EBSD datasets were refined by dilating the grains in a single iteration. The EDS datasets were corrected for signal shifting relative to the EBSD image that was due to the relative positioning of the EDS detector to the EBSD detector. Representative EBSD and EDS micrographs were selected after imaging three locations on five samples of each composition. EBSD micrographs of LLZO-Al0.45 and LLZO-Al0.55 were artificially lightened to improve visibility. The median grain boundary misorientation angle and grain size information is that of representative samples. All samples were stored in an argon filled glove box (Omni-Lab, VAC) with less than 1 ppm of oxygen to minimize atmospheric exposure.

2.2. Materials characterization

2.2.1. X-ray diffraction (XRD)

XRD (Miniflex 600, Rigaku) was used to determine the crystalline phases present after hot-pressing. To gain a qualitative understanding of phase purity across all samples, Cu Kα radiation was used to collect a spectrum from 15 to 60° 2θ at a rate of 5° min^{-1} on each produced pellet. To obtain quantitative phase purity information, a representative pellet from each composition was ground into powder to minimize differences in spectra due to pellet height variation and processing-induced stress. Cu Kα radiation was used to collect a spectrum from 15 to 60° 2θ at a rate of 4° min^{-1}. Rietveld refinement was then performed on these spectra to quantify the amount of each secondary phase present in each sample composition using Rigaku PDXL 2.8 integrated X-ray powder diffraction software.

2.2.2. Scanning electron microscopy (SEM)

To analyze the microstructure, SEM was performed on polished surfaces and fracture surfaces of the LLZO pellets using a Hitachi TM3030 Tabletop Microscope. The percent porosity was calculated by measuring the area of the porous regions of the polished surface with ImageJ software and dividing that by the total area of the image. This measurement was averaged over three locations on each sample, then averaged over five samples for each composition.

2.2.3 Time-of-flight secondary ion mass spectrometry (TOF-SIMS)

TOF-SIMS analysis was performed by using TOF-SIMS V system (ION-TOF GmbH, Münster, Germany). The measurements were done in a dual beam setting[50] in non-interlaced mode[51]. For the materials erosion, a 1 keV oxygen ion beam was rasterized over an area of 300 × 300 μm^2. For generation of analyzed secondary ions, a focused 25 keV Bi3 ion beam was used and the Bi ion gun was operated in the high current bunched mode. The analyzed area was 50 × 50 μm^2 and centered within the sputter crater to avoid crater edge effects. Between the sputtering and analysis pulses, a low energy (20 eV) electron flood gun was used to compensate for sample charging during the sputter processes. The data analysis was carried out by using Software package SurfaceLab 6 (ION-TOF GmbH).

2.3. Electrochemical characterization

Electrochemical impedance spectroscopy (EIS) was performed on three hot-pressed pellets at each composition at nominal temperatures of -16^{o} C, -11^{o} C, -8^{o} C, -5^{o} C, and 23^{o} C to determine the bulk and grain boundary activation energy. In order to perform low temperature measurements, samples were placed in a freezer (1.1 Cu Ft Upright Freezer, Northair) with an adjustable temperature dial. A thermocouple was attached to each side of the fixture in which the sample was being tested. The resulting temperatures as read from the thermocouples were averaged together to determine the temperature at which the EIS was performed. EIS was also performed on five pellets at a nominal temperature of 23^{o}C to calculate averages of bulk and total ionic conductivity as well as percent grain boundary resistance. Gold electrodes were sputter coated on both sides of each pellet using a sputter coater (Desk V, Denton Vacuum). EIS measurements were performed from 7 MHz to 1 Hz. The perturbation amplitude varied between 10 mV and 300 mV, depending on the ionic resistance of the sample. A Bio-Logic VMP300 and EC-Lab V11.33 software were used to conduct the EIS measurements. A modified equivalent circuit developed by Huggins was used for modeling the data and determining the bulk, grain boundary, and total resistance.[52] Bulk conductivity was calculated using the bulk resistance from the EIS measurements, specific specimen thickness, and electrode area. Total conductivity was calculated using the combined bulk and grain boundary resistance from the EIS measurements, specific specimen thickness, and electrode area. The percent grain boundary resistance was calculated using the following equation:

$$\%\,Grain\ Boundary\ Resistance = \frac{100 * Grain\ Boundary\ Resistance}{Grain\ Boundary\ Resistance + Bulk\ Resistance} \tag{1}$$

As stated above, Arrhenius measurements were conducted to determine an activation energy for each composition from three samples measured at all five nominal temperatures. The grain boundary resistance activation energy was calculated from the following equation:

$$\ln\left(T/(R * A_{electrode}\right) = \ln\left(R_0 * A_{electrode}\right) - E_{gb}/k \tag{2}$$

where T is temperature in Kelvin, R is grain boundary resistance, $A_{electrode}$ is the area of the electrode, R_0 is a constant, E_{gb} is the grain boundary activation energy, and k is the Boltzmann constant.

The bulk conductivity activation energy was calculated from the following equation:

$$\ln(\sigma_b T) = \ln(\sigma_{b0}) - E_b/kT \tag{3}$$

where σ_b is the bulk conductivity, σ_{b0} is a constant, and E_b is the bulk activation energy.

3. Results and Discussion

3.1. Phase purity and microstructure as a function of aluminum concentration

3.1.1. Phase purity and density

To determine the phase purity as a function of aluminum concentration, XRD was conducted for hot-pressed pellets from each composition in both pellet form (Figure 1a) and pulverized pellet form (Figure 1b). Samples of all four aluminum concentrations have cubic LLZO phase stability both before and after hot-pressing (Figure S1, Figure 1, Table 1). The observation of cubic LLZO in these compositions agrees with findings by several other works.[21,23,36,37] In general, both the pellets and the pulverized pellets show the same phases, though the slight variations in secondary phase intensity between the two may be due to inhomogeneous distribution of the secondary phases in the pellets. All secondary phases present in the pellets, with the exception of $La_2Zr_2O_7$, were already present in the calcined powders (Figure 1, Figure S1). However, the calcined powders had additional secondary phases beyond those also present in the hot-pressed pellets (Figure S1, Figure 1). This reduction in secondary phases after hot-pressing is potentially a result of re-homogenization during the hot-pressing process.

There are subtle differences between the LLZO-Al0.25, LLZO-Al0.35, and LLZO-Al0.45 hot-pressed sample XRD spectra with regards to secondary phases. The secondary phase that is present, $La_2Zr_2O_7$, is often observed and of small concentrations.[21,37,53] The small amount of $La_2Zr_2O_7$ in the LLZO-Al0.35 composition (3.2 wt.%) is a common side effect of lithium deficiency (Figure 1, Table 1).[37,53] Since no excess lithium was added to this powder prior to calcination and it contained less stoichiometric lithium than LLZO-Al0.25, $La_2Zr_2O_7$ could have formed at this composition due to lithium loss while LLZO-Al0.25 and LLZO-Al0.45 maintained phase purity.

The only substantial formation of secondary phases after hot-pressing occurred in the LLZO-Al0.55 composition (Figure 1, Table 1). The increased concentrations of secondary phases are visible in the pellet and powder XRD and the surface SEM (Figure 1, Figure 2). Through Rietveld refinement of the XRD powder spectra, three different secondary phases were identified. They were later confirmed by EDS analysis (Figure 2, Figure 5). These phases were $LaAlO_3$ (2.9 wt.%), $La_2Zr_2O_7$ (9.6 wt.%), and Li_2ZrO_3 (2.9 wt.%) (Figure 1, Table 1). In other studies, increased concentrations of aluminum also lead to the formation of $LaAlO_3$ and $La_2Zr_2O_7$ but not Li_2ZrO_3.[19,21,36,37] It is believed that the formation of the $LaAlO_3$ phase is related to the aluminum solubility limit in the LLZO. In LLZO, aluminum preferentially substitutes for lithium at the 24d tetrahedral site, and secondarily in the 96h and 48g sites.[19,23,42,45,54] It is believed that once the energetically favorable sites have been filled to their maximum aluminum capacity and the solubility limit is reached, the excess aluminum forms aluminum-rich secondary phases, such as $LaAlO_3$.[21,37] As was mentioned above, it is commonly observed that $La_2Zr_2O_7$ forms due to lithium loss.[37,53] Similar to the LLZO-Al0.35 and LLZO-Al0.25 compositions discussed above, the overall amount of stoichiometric lithium of LLZO-Al0.55 was less than that of the LLZO-Al0.45 sample, even though the same amount of excess lithium was present. This decrease in lithium concentration could have led to $La_2Zr_2O_7$ formation through lithium loss in the LLZO-Al0.55 composition. $La_2Zr_2O_7$ may also have formed via reaction pathway. According to Wolfenstine, *et. al.*, the addition of Al_2O_3 to LLZO leads to the formation of both $La_2Zr_2O_7$ and Li_2ZrO_3.[55] Therefore, the excess Al_2O_3 in the LLZO-Al0.55 composition may have reacted with the LLZO, serving as a possible mechanism for the formation of both of these phases. As an alternative explanation, it has been proposed that when aluminum substitutes into the tetrahedral sites adjacent to lanthanum and zirconium sites, it becomes energetically favorable for lanthanum and zirconium vacancies to form.[37] In order to ensure charge balance, lithium simultaneously forms a vacancy when the zirconium vacancy is formed.[37] Therefore, it seems possible that as aluminum doping increases, lanthanum, zirconium, and lithium all increasingly precipitate out of the garnet structure, potentially explaining why $LaAlO_3$, $La_2Zr_2O_7$, and Li_2ZrO_3 form with increased aluminum concentrations.

In the XRD patterns of pellets with LLZO-Al0.25 and especially LLZO-Al0.35 compositions, there are atypical relative intensity ratios when compared to the pattern from the Inorganic

Crystal Structure Database (ICSD) (Figure 1, red boxed regions). No noticeable variations were observed in the patterns of the pulverized pellets of the LLZO-Al0.25 samples, but they were observed in those of the LLZO-Al0.35 samples (Figure 1). The expected relative intensity heights shown by the ICSD patterns are defined by samples with completely random grain orientations. Variations in the relative intensity heights, therefore, indicate a degree of non-random orientation in the samples. Non-random orientation can be due to texturing. In texturing, a majority of the grains adopt a few specific crystallographic orientations. Non-random orientation can also be due to abnormal grain growth. With abnormal grain growth, the few larger grains will dominate the diffraction spectra. Since the garnet crystal structure is cubic, grinding could decrease the observation of texturing or abnormal grain growth in the resulting XRD patterns by re-randomizing the individual grains. Based only on the XRD, it is not possible to determine whether the atypical relative intensities are due to texturing or abnormal grain growth. Therefore, an EBSD investigation was conducted to determine what phenomena caused the relative intensity variation of the LLZO-Al0.25 and LLZO-Al0.35 compositions, and to better understand the effects of different aluminum concentrations on the microstructure (i.e., grain size) and grain boundary misorientation angles (Figure 3).

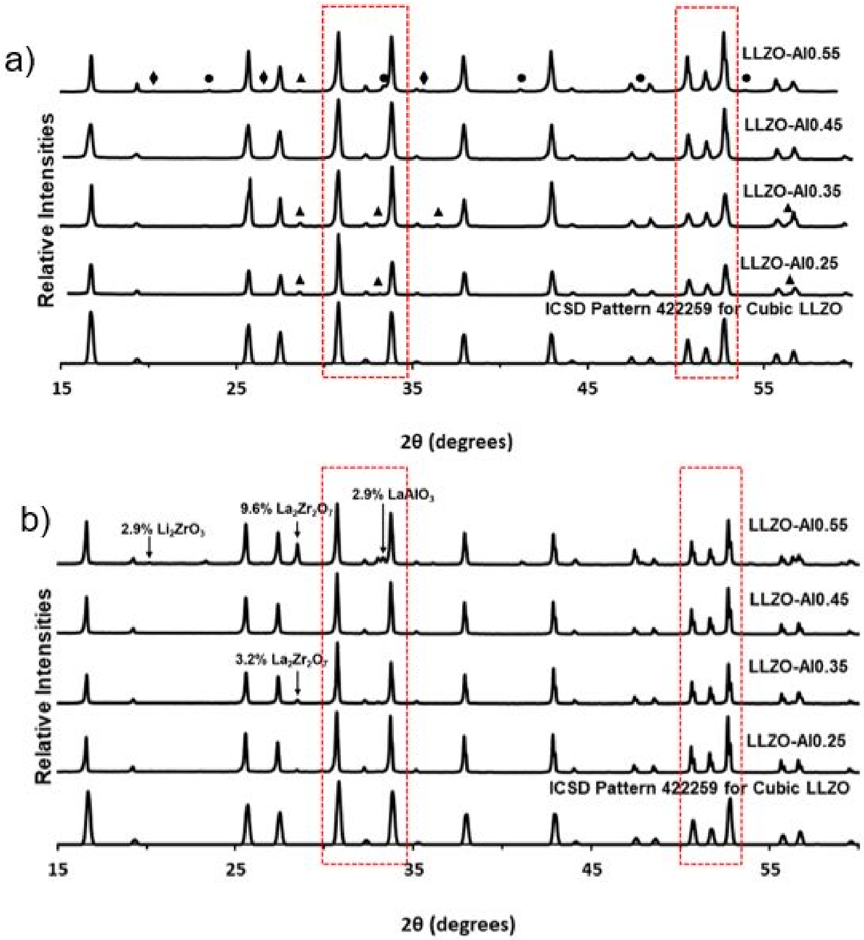

Figure 1: a) Representative XRD patterns of LLZO-Al0.25, LLZO-Al0.35, LLZO-Al0.45, and LLZO-Al0.55 hot-pressed pellets. ICSD Pattern 422259 was used for cubic LLZO. Impurity phases are indicated by: ▲ $La_2Zr_2O_7$, ● $LaAlO_3$, and ♦ Li_2ZrO_3. b) XRD spectra of pulverized hot-pressed pellets of LLZO-Al0.25, LLZO-Al0.35, LLZO-Al0.45, and LLZO-Al0.55. The highest relative intensities of each present secondary phases are marked with arrows and the weight percentages of the secondary phase as determined by Rietveld refinement. Weight percentages are also reported in Table 1.

3.1.2. Microstructure as a function of aluminum concentration

Secondary electron microscopy (SEM) of polished surfaces of pellets from each aluminum concentration was performed to determine porosity and corroborate secondary phase findings of the XRD (Figure 2). All four compositions were highly dense, exhibiting less than 1.7% porosity (Figure 2, Table 1). The secondary phases are visible in the surface SEM and support the findings of the pellet and powder XRD (Figure 1, Figure 2). Phase identification is later confirmed with EDS (Figure 5).

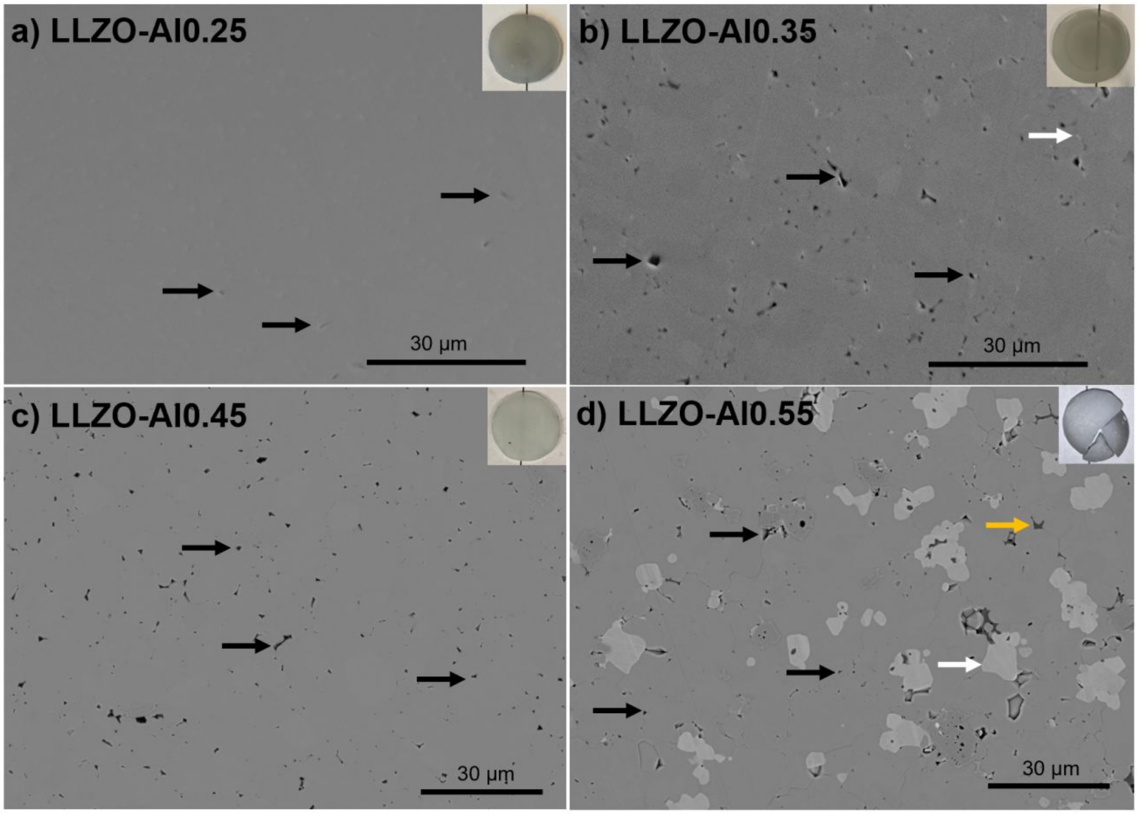

Figure 2: Representative secondary electron SEM images of polished, hot-pressed surfaces of a) LLZO-Al0.25, b) LLZO-Al0.35, c) LLZO-Al0.45, and d) LLZO-Al0.55. Black arrows indicate pores, white arrows indicate suspected $LaAlO_3$, and orange arrows indicate either the $La_2Zr_2O_7$

or Li_2ZrO_3. Insets are representative optical images of hot-pressed LLZO pellets (12.7 mm in diameter). Black lines are under each of the pellets to show variations in optical transparency.

In addition to SEM, EBSD was also performed on the surfaces of hot-pressed pellets of each aluminum concentration (Figure 3, Figure 4). From the EBSD, the grain orientation, morphology, and size along with the grain boundary misorientation angle can be determined (Figure 3, Figure 4). The grain orientation appears to be random for all compositions tested, indicating that no texturing is present (Figure 3). Random, untextured grains in hot-pressed LLZO are consistent with Sharafi, *et. al*.[56] Therefore, the relative intensity height variation observed in XRD for LLZO-Al0.25 or LLZO-Al0.35 cannot be due to texturing. Looking at grain size from the EBSD micrographs, LLZO-Al0.25, LLZO-Al0.45, and LLZO-Al0.55 are similar, while LLZO-Al0.35 often has a combination of small grains with a few comparably large grains (>100 μm) (Figure 3). When grain size distributions were quantified, all aluminum concentrations had similar grain sizes of 5-7 μm, although LLZO-Al0.55 had a large standard deviation due to the inclusion of secondary phase precipitates in the grain size calculations (Figure 4, Table 1). Due to the few extremely large grains (0.4% of the number of total grains taking up >50% of the area in Figure 4b), LLZO-Al0.35 has a larger standard deviation in grain size measurements than the samples of other aluminum concentrations (Table 1). Similar grain size results were also observed in the fracture analysis (Figure S2). The apparent distribution of many small and fewer large grains is characteristic of abnormal grain growth.[57] The lack of texturing and the observation of abnormal grain growth in the EBSD make it clear that the irregular relative intensities in the pellet XRD spectra (Figure 1) can be attributed to abnormal grain growth. It is unclear why abnormal grain growth seems to favor LLZO-Al0.35 over the other compositions. Possible mechanisms for abnormal grain growth, particularly with this composition, will be explored in a future work.

In addition to grain size, the grain boundary misorientation angle was also analyzed using EBSD (Figure 4). There is a wide spread of misorientation angles (1-65^o) in all samples, with higher misorientation angles being more favorable than lower ones. More than half of the grain boundary misorientation angles were greater than 41^o in LLZO-Al0.25, LLZO-Al0.35, and LLZO-Al0.45 and greater than 35^o in LLZO-Al0.55. Sharafi, *et. al.* found in their study that samples of LLZO-Al0.25 processed at similar hot pressing temperatures had a similar median grain boundary misorientation angle of 35^o.[56] The high median misorientation angles mean that there is a large fraction of high angle grain boundaries in LLZO among all aluminum concentrations tested. Misorientation angle distributions with high fractions of high angle grain boundaries are typical of oxide materials.[57] Overall, the grain boundary misorientation angle does not seem to be significantly affected by aluminum concentration.

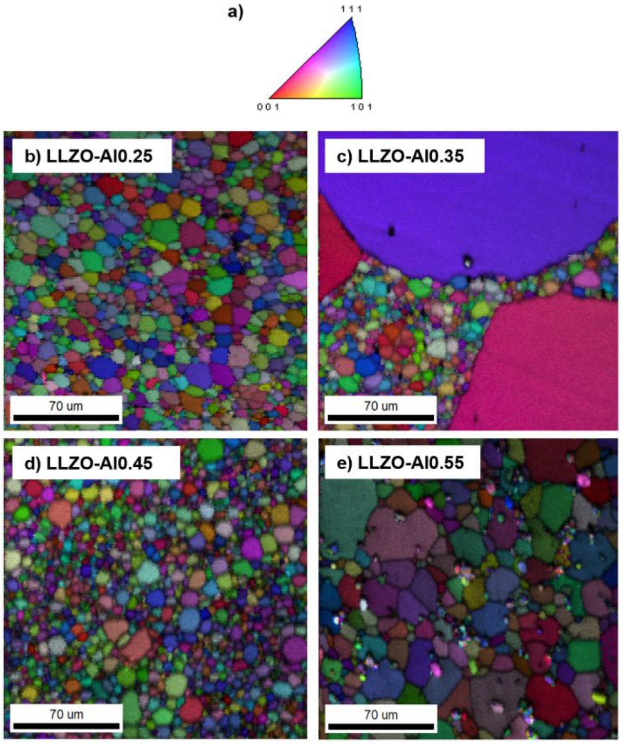

Figure 3: Representative EBSD grain orientation maps overlaid with image quality maps of polished LLZO surfaces. a) Correlation between color and crystallographic orientation. b), c), d), e) EBSD of LLZO-Al0.25, LLZO-Al0.35, LLZO-Al0.45, and LLZO-Al0.55, respectively.

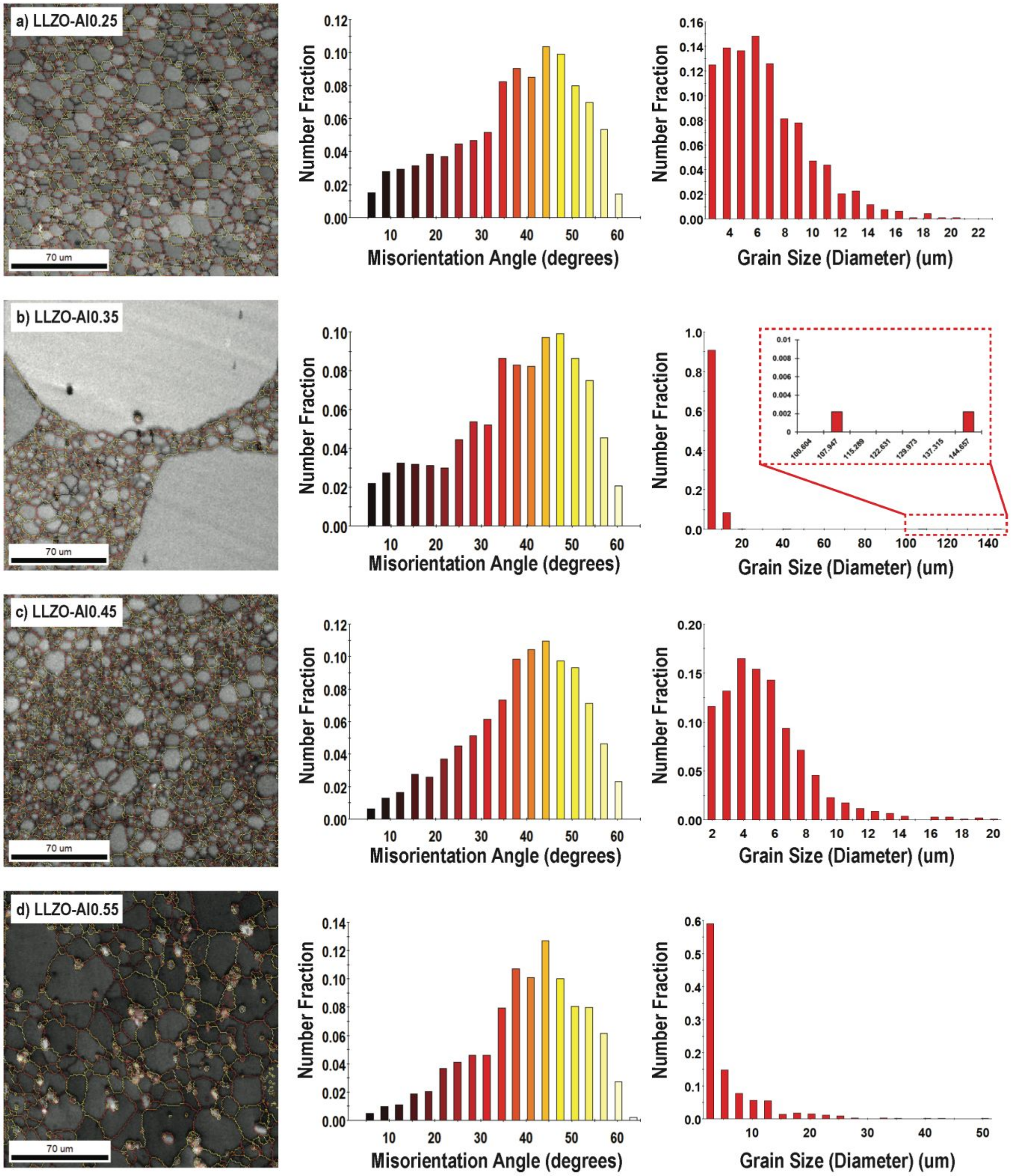

Figure 4: The first column shows representative grain boundary misorientation angle maps over image quality maps. The colors over the grain boundaries represent the misorientation angles defined in the corresponding misorientation histograms in the second column. The third column

shows the corresponding grain size distribution. a) LLZO-Al0.25, b) LLZO-Al0.35, c) LLZO-Al0.45, d) LLZO-Al0.55.

3.2. Phase purity as a function of microstructure

To corroborate the XRD and SEM analysis and to further investigate the secondary phase formation as a function of microstructure, EDS and TOF-SIMS were performed on hot-pressed pellets of each aluminum concentration (Figure 5, 6). The EDS map for each detectable element was overlaid on an EBSD image quality map to better identify the element distribution as a function of microstructure. Consistent with the XRD analysis (Figure 1), secondary phases are evident in the TOF-SIMS and EDS data for the LLZO-Al0.55 composition, while few to no secondary phases are observed in the EDS of the LLZO-Al0.25, LLZO-Al0.35, and LLZO-Al0.45 samples. Similarly, the TOF-SIMS elemental mappings of the LLZO-Al0.25 and LLZO-Al0.35 samples (Figure 6a and b) show identical aluminum, zirconium, and lanthanum positions, with only a very slight deviation in the lithium signal outside of regions of high lithium and low aluminum, zirconium, and lanthanum signal. These regions with increased lithium and decreased aluminum, zirconium, and lanthanum concentrations are commonly observed in LLZO samples prepared in ambient atmosphere and indicate areas where LiOH and Li_2CO_3 have formed.[58–60] The areas are localized and are often, but not necessarily, associated with small cracks or pores, but since TOF-SIMS intensity is not indicative of the concentration, further analysis is difficult. However, it suggests that few to no secondary LLZO phases are seen in the TOF-SIMS plots of LLZO-Al0.25 and LLZO-Al0.35 samples. Interestingly, unlike XRD and EDS, the TOF-SIMS plot for LLZO-Al0.45 shows some aluminum segregation, which occurs preferentially between grains and at grain boundaries (Figure 6c). Some of these precipitates have lower lanthanum content (Figure 6c, white circles), indicating the onset of secondary phase formation that is too low to be detected in XRD and EDS. In addition, the zirconium map looks more homogeneous than the lanthanum map, suggesting that these precipitates are indicative of lanthanum-poor regions (e.g., Li_2ZrO_3). However, since the intensities in TOF-SIMS are also dependent on the matrix of the measured ion, the exact composition cannot be determined.

Finally, both the EDS and TOF-SIMS of the LLZO-Al0.55 sample show clear regions of different elemental composition, especially at the grain boundaries and triple points of LLZO. In Figure 6d, the lanthanum map shows three distinct regions, of low (black), medium (orange) and high (yellow) intensity. While the black region indicates a pore that is also present in the aluminum and zirconium map, the orange region (marked with a white arrow) has a much lower aluminum signal and indicates the $La_2Zr_2O_7$ secondary phase forming adjacent to the aluminum stabilized LLZO phase (yellow). Similar results were also observed in EDS (Figure 5d). Unfortunately, the lithium signal in TOF-SIMS was very low for both the LLZO-Al0.45 and LLZO-Al0.55 samples, but the size of the precipitate in the LLZO-Al0.55 sample, around 15 μm, agrees well with the size observed in SEM/EDS images of the same composition in Figures 5d and 2d. Additionally, EDS of LLZO-Al0.55 indicates secondary phases with decreased zirconium concentration and secondary phases with decreased lanthanum concentration, suggesting the formation of $LaAlO_3$ and Li_2ZrO_3 (Figure 5d). Thus, our TOF-SIMS results and the relative intensities of the EDS spectra for each element confirm the observations by XRD and previous work that the secondary phases that form at higher aluminum concentrations are $La_2Zr_2O_7$, $LaAlO_3$, and Li_2ZrO_3.[21,61]

As mentioned above, secondary phases in the LLZO-Al0.45 and LLZO-Al0.55 composition are preferentially located at the grain boundaries (Figure 5, 6). Using backscatter SEM, Geiger, *et. al.* also found that the secondary phase $LaAlO_3$ was present at the grain boundaries of their samples, albeit in samples with lower aluminum concentrations.[19] Gao, *et. al.* calculated that it was possible for $LaAlO_3$ to form at the grain boundaries, as well.[42] With this in mind, the increased presence of secondary grain boundary phases appears to be the cause of the increased observation of intergranular fracture at the LLZO-Al0.55 composition as compared to the largely intragranular fracture in the other three compositions (Figure S2). Larger concentrations of these phases appear to result in weaker grain boundary adhesion and more facile grain boundary fracture. In the case of the LLZO-Al0.45 and LLZO-Al0.55 composition, the increased concentration of secondary phases could have led to grain boundary pinning or drag, where secondary phases or solutes impede grain boundary movement. The increased occurrence of secondary phases may have led to an increased grain growth obstruction over a larger, more uniform cross-section of grains, ultimately deterring the abnormal growth. In comparison, the secondary phase in the LLZO-Al0.35 is located within the abnormal grain. The location of the secondary phase may be due to the rate of grain boundary movement during abnormal grain growth. The grain boundary of the abnormal grain may have overcome the small concentration of the secondary phase so that it is trapped in the abnormal grain rather than at the grain boundary.

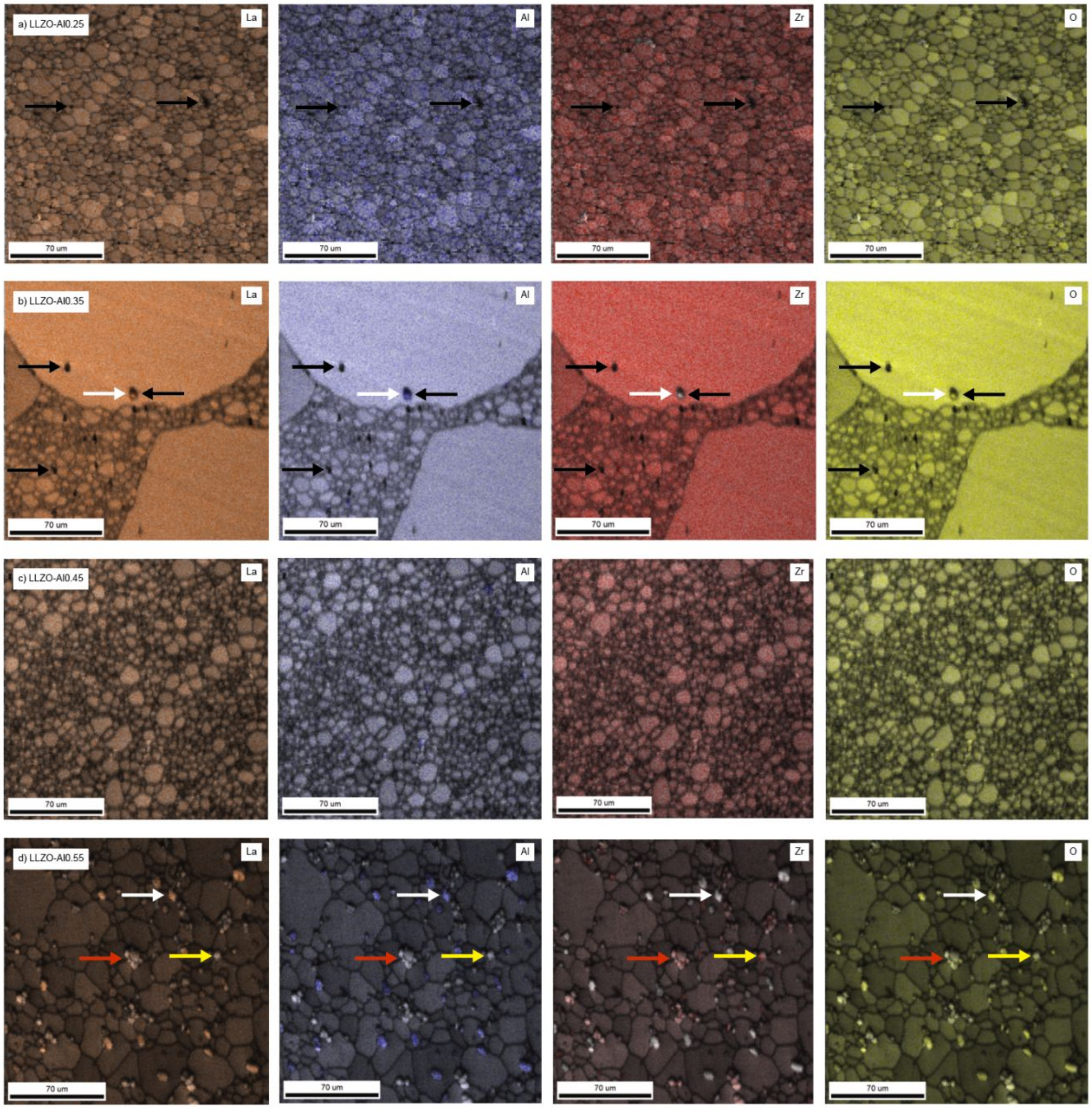

Figure 5: Representative EDS mapping over image quality maps of polished surfaces of a) LLZO-Al0.25, b) LLZO-Al0.35, c) LLZO-Al0.45, d) LLZO-Al0.55. Black arrows indicate pores, red arrows indicate suspected $La_2Zr_2O_7$, white arrows indicate suspected $LaAlO_3$, and yellow arrows indicate suspected Li_2ZrO_3. The more prominent the color the more prominent the element.

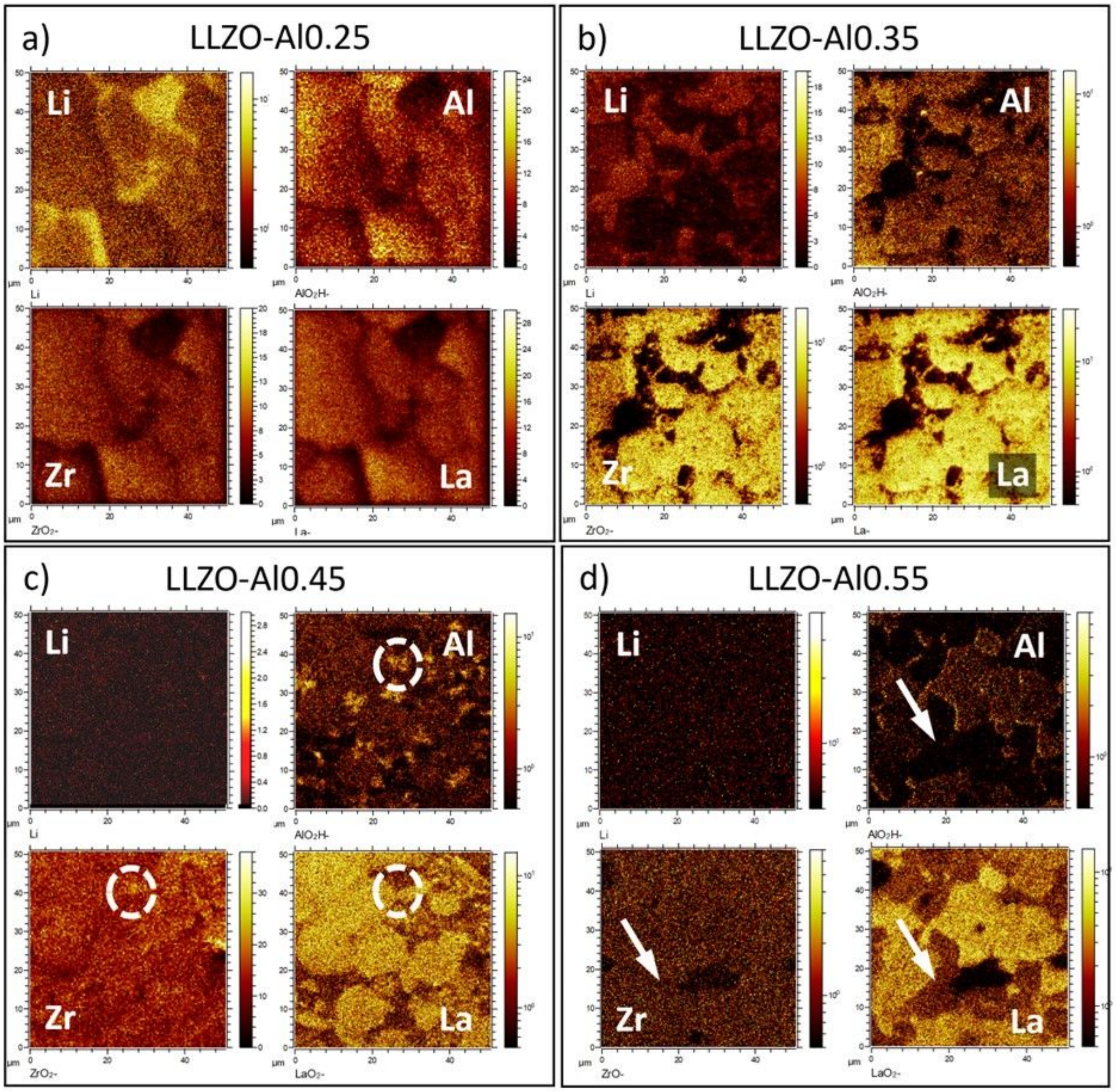

Figure 6: TOF-SIMS intensity plots of lithium, aluminum, zirconium, and lanthanum for a) LLZO-Al0.25, b) LLZO-Al0.35, c) LLZO-Al0.45, d) LLZO-Al0.55. White circles in c) and white arrows in d) are at exactly the same position in each image. Lithium count rate for c) and d) was very low.

In one case, it was possible to correlate zirconium-poor phases directly with the grain boundaries of an abnormal grain (Figure 7). Comparing the EBSD and EDS maps, it can be seen that the zirconium content decreased along the grain boundary of the abnormal grain, while lanthanum, aluminum, and oxygen remained present. These data suggests that there is a phase containing lanthanum, aluminum, and oxygen along the grain boundaries. Given the previous analysis, we believe that this could be the $LaAlO_3$ phase detected in the XRD and EDS (Figure 1, Figure 5, Table 1). However, due to the inability for EDS to detect lithium, it was not possible to determine if lithium was also present at the grain boundary. Regardless, the presence of the secondary grain boundary phase suggests that an aluminum-based phase aids the abnormal grain growth through increased mass transport to abnormal grains or through solute drag and pinning of less mobile grain boundaries. Geiger, *et. al.* also saw increased aluminum concentrations at the edges of grains and very small grains of $LaAlO_3$ and La_3AlO_6 at the grain boundaries in samples of similar aluminum concentrations.[19] Gao, *et. al.* also calculated that aluminum segregation and aluminum-rich secondary phase formation was possible in the grain boundaries.[42] At this point, it is not possible to determine whether this boundary phase enabled the abnormal grain growth as a solid or as a liquid. However, if it is a liquid phase, it could not be a pure La-Al-O phase, since no liquid forms below 1791^{o}C, which is over 500^{o}C more than the hot-pressing temperature.[62] There is no known phase diagram or investigation into the liquidus of the Li-Al-La-O quaternary system, so it is not known if a liquid phase is possible under hot-pressing conditions or if the grain boundary phase of the abnormal grain is solid during sintering and densification. Although this was the only case where this phenomenon was recorded, it could be that it occurred at other abnormal grain boundaries below the detection limits of the SEM EDS. It would be helpful to supplement the SEM EDS with TEM EDS to allow for higher resolution characterization. TEM analysis could help to determine experimentally if the presence of secondary phases at the grain boundaries of abnormal grains is common, what phases are present, and if there are grain boundary impurities.

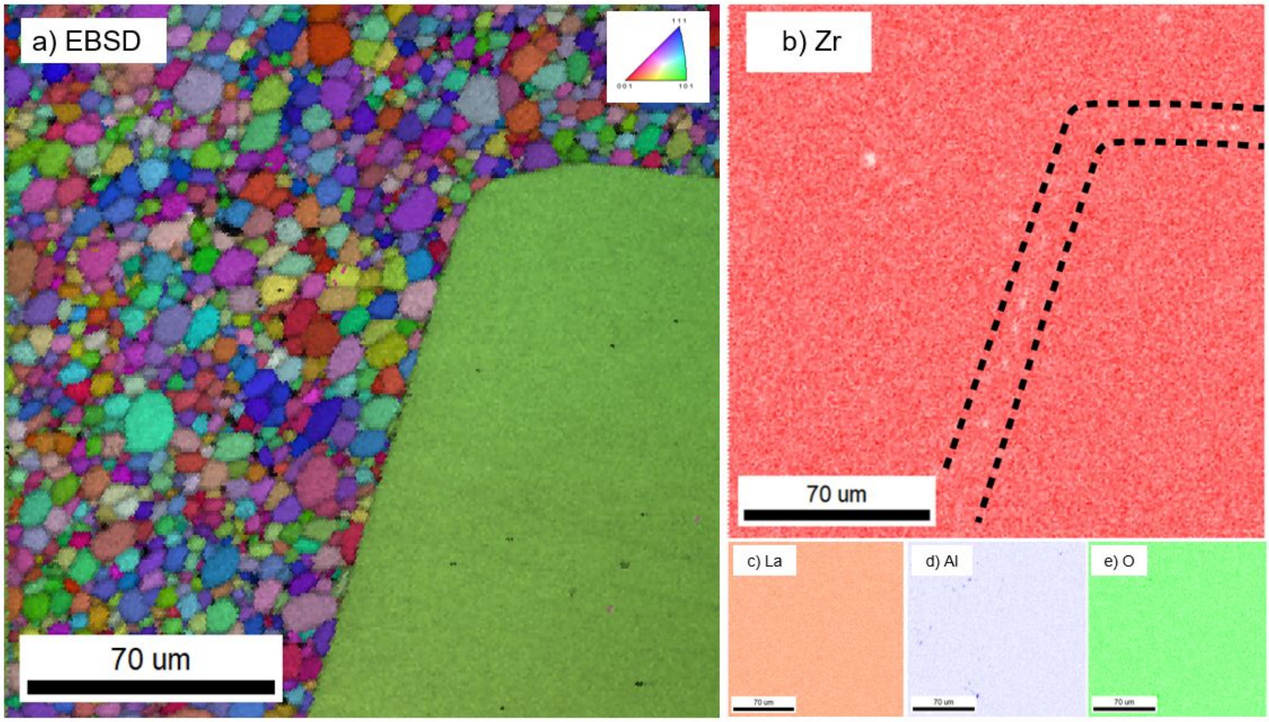

Figure 7: a) EBSD image of abnormal grain growth in LLZO-Al0.25. Inset coordinates color with crystallographic direction. b), c), d), and e) are EDS maps of zirconium (Zr), lanthanum (La), aluminum (Al), and oxygen (O) of the same area as a). The more prominent the color the more prominent the corresponding element in each map. Black lines in b) surround the line of decreased zirconium concentration in the micrograph, which aligns with the grain boundary of the large grain in a).

3.3. Electrochemical characterization as a function of aluminum concentration

To determine the effects of aluminum concentration and microstructure on conductivity, EIS was performed on hot-pressed samples from each aluminum concentration. Figure 8 shows representative Nyquist plots obtained from the EIS at room temperature. Figure S3 shows the modified Huggins equivalent circuit that was used to decouple the bulk and grain boundary components of the resistance and an example of a Nyquist plot demarcated with the contributions of the grain, grain boundary, and electrode-electrolyte interface as determined by the equivalent circuit. There is a clear effect of aluminum concentration on conductivity. As the aluminum concentration increases, the bulk conductivity decreases (Figure 8, Figure 9, Table 2). This agrees with previous findings by Sudo, *et. al.* at and above 0.247 mol of aluminum.[38] The average bulk conductivity values are 0.56 mS/cm, 0.33 mS/cm, 0.28 mS/cm, and 0.15 mS/cm for LLZO-Al0.25, LLZO-Al0.35, LLZO-Al0.45, and LLZO-Al0.55, respectively (Figure 9, Table 2). LLZO-Al0.25 values align well with the literature data on hot-pressed samples of this composition.[56] In LLZO, the added aluminum substitutes preferentially to the lithium site, as stated above. When it is substituted into a lithium site in the lattice, it creates two lithium vacancies to ensure charge balance. Therefore, each additional aluminum added leads to three fewer lithium-ions in the lattice. If fewer lithium-ions are available to diffuse through the LLZO, the lithium-ion conductivity of the LLZO will be lowered, as dictated by the following equation derived from the Nernst-Einstein relation:

$$\sigma_b = N\ e\ \mu \tag{4}$$

where N is the number of charge carriers, e is elementary charge, and μ is the mobility of the charge carrier. Therefore, as increased concentrations of aluminum are added to the lattice, the lithium-ion concentrations will decrease and the bulk conductivity will decrease accordingly. The only exception to the decrease in bulk conductivity is between LLZO-Al0.35 and LLZO-Al0.45, both of which are within a standard deviation of the same bulk conductivity. This discrepancy could be due to the 10 mol% lithium-excess in LLZO-Al0.45, which increases the carrier concentration of lithium ions to high enough concentrations to both prevent the formation of $La_2Zr_2O_7$ and compensate for the number of lithium ions that would have been lost due to aluminum doping. It could also be that the solubility limit of aluminum is near these concentrations. Once the solubility limit is exceeded, the bulk conductivity will remain reasonably constant while the secondary aluminum phases begin to form. Since aluminum-rich secondary phases began to form at LLZO-Al0.45 (Figure 6), it may be that the maximum aluminum solubility and minimum bulk conductivity were reached between the LLZO-Al0.35 and LLZO-Al0.45 compositions, leading to the similar reported bulk conductivity values (Figure 9, Table 2). While it is not entirely clear why there is a further decrease in bulk conductivity of the LLZO-Al0.55 after the apparent surpassing of the solubility limit, it may be due to the significant increase in secondary phase concentrations (Figures 1, 2, 5, 6, Table 1) that could lead to decreased area for conduction as well as increased tortuosity, both of which could lead to a decrease in bulk conductivity. In addition, at the LLZO-Al0.55 composition, it is observed that Li_2ZrO_3 formed, which reduces the amount of lithium in the lattice, and a significant amount of $La_2Zr_2O_7$ formed, which results from lithium loss from the lattice. Thus, the formation of these phases suggests a reduction in the lithium carrier concentration in the lattice of the LLZO-Al0.55 composition and, hence, bulk conductivity to a value lower than expected.

Grain boundary resistance at room temperature, as determined by fitting of the EIS spectra, was used to calculate the percent grain boundary resistance (grain resistance to total resistance) as detailed in Equation 1 in the experimental section (Figure 9, Table 2). The percent grain boundary resistances of LLZO-Al0.25 and LLZO-Al0.35 samples were all within a standard deviation, indicating similar grain boundary composition and structure (Table 2). The difference in grain size distribution may have affected the percent grain boundary resistance of the LLZO-Al0.35, as larger grains may correlate with fewer grain boundaries per area compared to the other compositions. However, since it is difficult to determine the location and number of the abnormal grains relative to the electrode, it is challenging to determine the magnitude of the effect. Given this difficulty and the fact that the average grain size in the LLZO-Al0.35 samples was similar to that of the other compositions, the effect of grain size on the percent grain boundary resistance cannot, in a first approximation, account for the difference in grain boundary resistance between the different aluminum concentrations. Regardless, the percent grain boundary resistance was significantly higher in the LLZO-Al0.55 composition compared to the other three compositions (Table 2). As all four compositions had similar levels of porosity, the difference in grain boundary resistance cannot be attributed to density variation (Figure 1, Table 1). Similarly, all investigated samples with different aluminum concentrations seem to have similar grain morphologies and grain boundary misorientation angles, so they cannot be responsible for the difference in grain boundary resistance in the LLZO-Al0.55 (Figure 3). It could be that the cause of the increased intergranular fracture in the LLZO-Al0.55 composition (Figure S2d) also led to increased grain boundary resistance. As seen in Figures 5 and 6, the intergranular fracture was apparently caused by secondary phases at the grain boundaries. The secondary phases present in the LLZO-Al0.55 composition have much lower or no lithium-ion conductivity compared to cubic LLZO.[63,64] Therefore, they may serve to insulate the grain boundaries and to prevent conductivity between the grains. The large standard deviation in the percent grain boundary resistance of LLZO-Al0.55 is due to one sample with a significantly higher percent grain boundary resistance than the others. Therefore, the very large standard deviation is due to the increased grain boundary resistance, and the LLZO-Al0.55 composition can still be considered to have the largest percent grain boundary resistance of all the compositions. Likewise, the small increase in percent grain boundary resistance in the LLZO-Al0.45 could also be due to the increase in resistive grain boundary secondary phases, as was observed in the TOF-SIMS analysis (Figure 6). The significantly decreased concentration of secondary phases in the LLZO-Al0.45 compared to the LLZO-Al0.55 correlates with the significant decrease in percent grain boundary resistance between the two compositions (Figures 1, 2, 5, 6, Table 1). Additionally, while there was a high concentration of secondary phases in the LLZO-Al0.35 (9.5 wt.%), the same increase in grain boundary resistance was not observed (Table 1). This could be due to the relative location of the secondary phases in the microstructure. Unlike LLZO-Al0.55 and LLZO-Al0.45, the secondary phases were located in the grains of the LLZO-Al0.35 microstructure rather than at the grain boundaries (Figure 5). Therefore, the secondary phases would not have had an effect on the grain boundary fracture or grain boundary resistance, as was observed for LLZO-Al0.55. Grain boundary impurities could have played a role in grain boundary resistance[42], but, given the resolution of our techniques, it is not possible to determine if they were present. Essentially, the bulk conductivity decreased with increasing aluminum concentration due to a decrease in lithium-ion charge carriers, while the percent grain boundary resistance appears to have increased at increased aluminum concentrations due to precipitation of high concentrations of ionically resistive secondary phases at the grain boundaries.

The combination of the bulk and grain boundary resistances determines the total conductivity of each composition. Total conductivity calculations are detailed in the experimental section. The average total conductivity values are 0.46 mS/cm, 0.27 mS/cm, 0.21 mS/cm, and 0.099 mS/cm for LLZO-Al0.25, LLZO-Al0.35, LLZO-Al0.45, and LLZO-Al0.55, respectively (Table 2), and reflect the trends of decreasing bulk conductivity and increasing grain boundary resistance with increasing aluminum concentration. As such, the LLZO-Al0.25 composition, with its combination of both low grain boundary resistance and the highest grain boundary conductivity, had the highest total conductivity of the four compositions. Similar trends of decreasing total conductivity with increasing aluminum concentration are observed by Jinn and McGinn and Sudo, *et. al.*, though exact conductivity values vary due to differences in microstructure (i.e., porosity).[36,38] In the case of Sudo, *et. al.,* the optimized conductivity in the cubic stability range was found at 0.247 mol of aluminum, with decreased conductivity values both below and above this concentration.

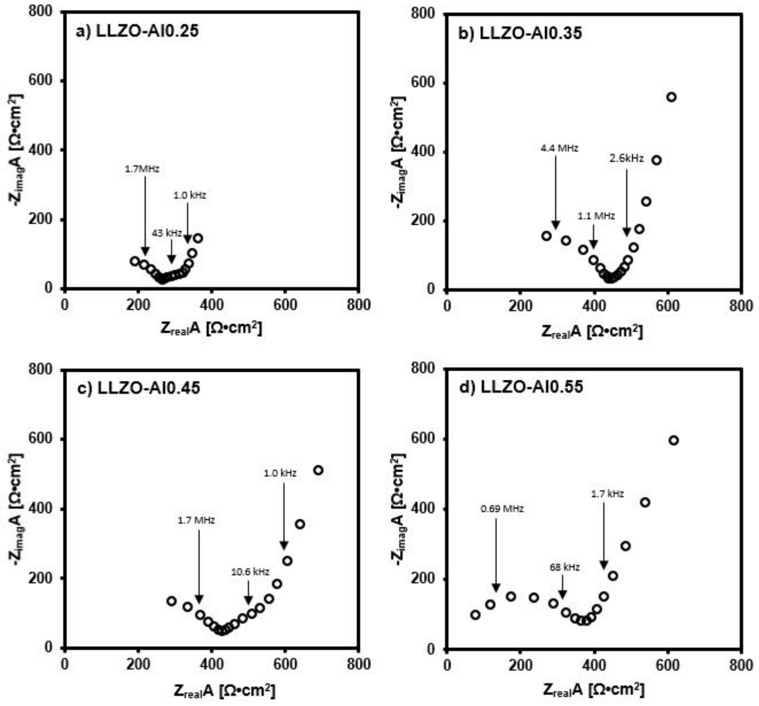

Figure 8: Representative Nyquist plots at room temperature obtained from EIS for a) LLZO-Al0.25, b) LLZO-Al0.35, c) LLZO-Al0.45, d) LLZO-Al0.55. Nyquist plots are annotated with characteristic frequencies obtained from equivalent circuit fitting.

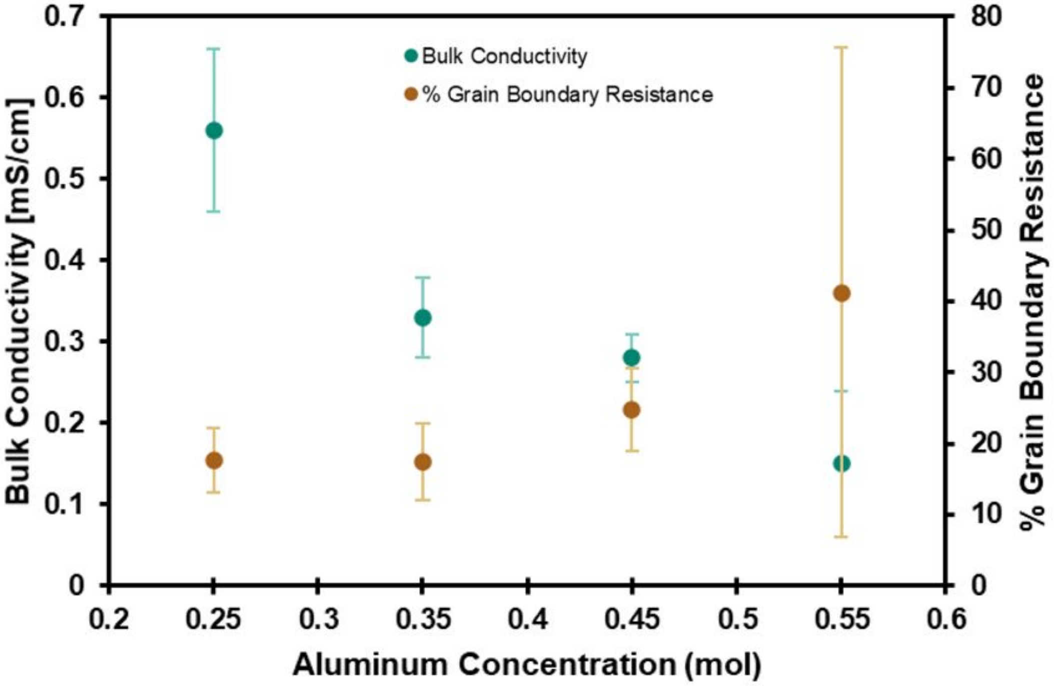

Figure 9: Bulk conductivity (blue) and percent grain boundary resistance (brown) as a function of aluminum concentration.

EIS was also performed as a function of temperature to determine the activation energy for lithium-ion conduction in the bulk and the activation energy for lithium-ion resistance in the grain boundaries of samples from each composition (Figure 10, Figure 11, Table 2). The activation energy for the process was determined from the slope of the line (Figure 10), as dictated in Equations 2 and 3 of the experimental section. Calculated values for the bulk and grain boundary activation energies for LLZO-Al0.25 (0.39 eV bulk, 0.47 eV grain boundary) are within a standard deviation or 0.01 eV from the standard deviation of previously reported values of hot-pressed LLZO-Al0.24 (0.36 eV bulk, 0.44 eV grain boundary) and LLZO-Al0.25 (0.36 eV bulk, 0.46 eV grain boundary) samples.[65,66] Arrhenius measurements that differentiate between bulk and grain boundary of the other aluminum concentrations are not known to the authors, so they cannot be compared to the obtained values. All bulk activation energies are within a standard deviation of each other. According to Mukhopadhyay, *et. al.*, aluminum substitution plays a few roles in the hopping of the lithium-ions through the bulk.[44] When in the lattice, aluminum blocks lithium interstitial sites, decreasing the hop frequency. Simultaneously, the aluminum opens nearby necks between hopping sites, increasing the ease of hopping, i.e., decreasing the activation energy of lithium mobility as aluminum concentration increases. However, based on the findings of this work it does not appear that the bulk activation energy changes in the range of aluminum concentrations tested. The activation energy for hopping is related to the bottle neck size for hopping between sites and hence, the lattice parameter.[67] From Table 1, it is observed that the lattice parameters (12.97-12.98 Å) are nearly independent of aluminum concentration, and hence, activation energy should be independent of aluminum concentration, which was observed. Hence, the mobility term in Equation 4 is roughly independent of aluminum concentration and, thus, the major variable controlling bulk conductivity is the lithium charge carrier concentration, which varies inversely with aluminum concentration.

We recognize that scatter was present in the grain boundary data to a greater degree than that of the bulk due to the limitations of fitting the smaller resistance of the grain boundary. This scatter was limited by decreasing the temperature during Arrhenius measurements and by using small electrode diameters, though not all scatter could be completely eliminated. For the grain boundary activation energy, LLZO-Al0.25, LLZO-Al0.45, and LLZO-Al0.55 all have activation energies within a standard deviation of each other (Table 2). Though LLZO-Al0.55 does have a much higher concentration of secondary phases at the grain boundary, these phases are largely blocking to lithium-ions. Therefore, lithium transport at the grain boundaries would be limited to sites that were not occluded by secondary phases and be much like the transport at the grain boundaries of LLZO-Al0.25 and LLZO-Al0.45. Thus, the transport properties would remain similar, leading to similar activation energies between the three compositions. Meanwhile, the LLZO-Al0.35 composition has a lower activation energy than the other compositions, though it is within a standard deviation of the LLZO-Al0.55 composition (Table 2). The change in activation energy at the grain boundaries of LLZO-Al0.35 is potentially related to ionically conducting secondary phases or impurities at the grain boundary. Based on the above microstructural evidence (Figures 5, 6, 7), it appears that different phases and different amounts of these phases are forming in the grain boundaries of the varying compositions. Therefore, the increased concentration of abnormal grains in LLZO-Al0.35 may help to define its unique activation energy. If secondary phases or solutes are present at the grain boundary, as was shown around the grain boundary of an abnormal grain in Figure 7, they may be altering the grain boundary structure and decreasing the activation energy for lithium-ion diffusion across the grains. If these phases are lithium-ion conductors, then the grain boundary transport will not be limited to the LLZO|LLZO grain interface, as may be the case for LLZO-Al0.55, thus causing a corresponding change in the grain boundary activation energy. The theorized sintering aid of $LiAlO_2$ may also play a role in both introducing abnormal grain growth and altering the activation energy of the grain boundary in LLZO-Al0.35.[36,39,43] The increased abnormal grain growth in conjunction with the decrease in activation energy may point to a difference in grain boundary character, either in composition or structure. However, it is not definitely known why there is a variation in the activation energy of the LLZO-Al0.35 grain boundaries or the origin of the abnormal grain growth. Though beyond the scope of this work, further investigation into the structure and electrochemical behavior of individual grain boundaries at each composition would be fruitful in discerning the cause of the difference between their activation energies and microstructures.

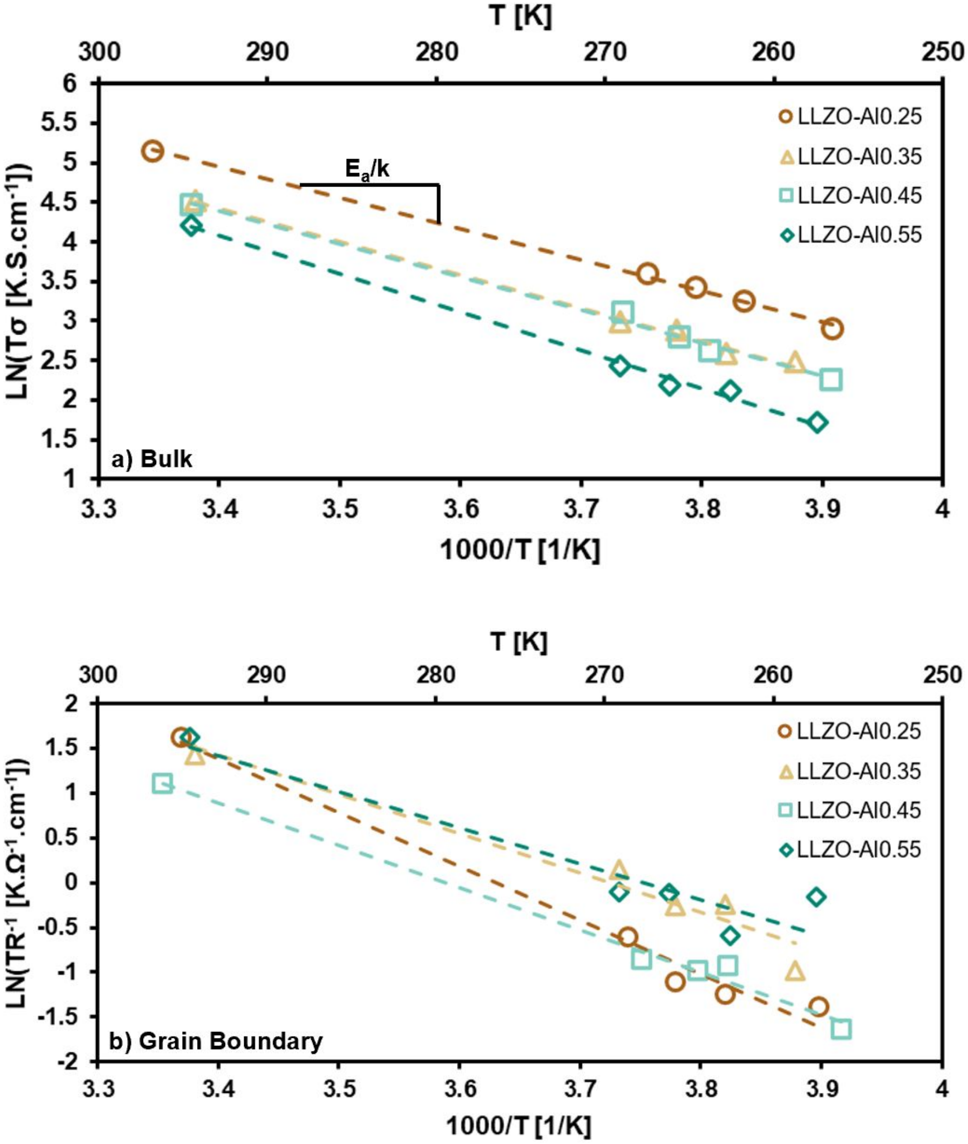

Figure 10: Conductivity as a function of temperature for a) bulk conductivity and b) grain boundary resistance. The activation energy is taken from the slope (E_a/k) of the best fit lines.

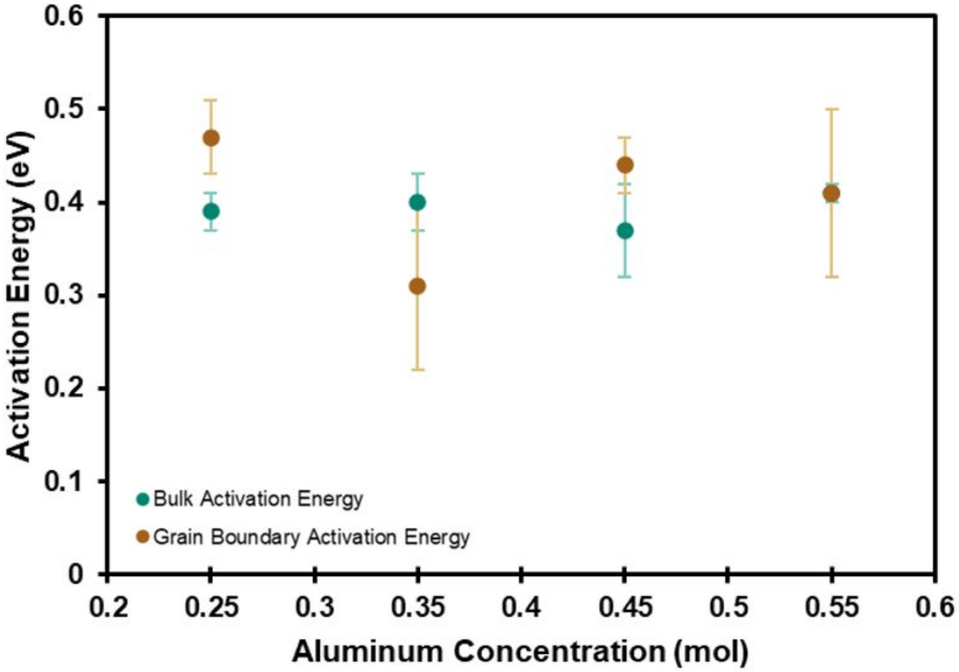

Figure 11: Bulk activation energy (blue) and grain boundary activation energy (brown) as a function aluminum concentration. The bulk and grain boundary activation energies are the same at the LLZO-Al0.55 composition, causing the data points to overlap.

Table 1: Summary of the structural and microstructural properties of LLZO-Al

Al concentration (mol)	Phase Purity (wt.%)	Lattice Parameters (Å)	Porosity (%)	d_{ave} (μm)	Median Misorientation Angle (°)
0.25	94.2% Cubic LLZO 4.1% Tetragonal LLZO	12.98	0.66±0.8	6.7±3.1	41
0.35	90.5% Cubic LLZO 6.3% Tetragonal LLZO 3.2% $La_2Zr_2O_7$	12.97	1.6±2.6	5.8±8.9	41
0.45	98.3% Cubic LLZO	12.97	1.0±0.7	5.3±2.7	41
0.55	84.3% Cubic LLZO 9.6% $La_2Zr_2O_7$ 2.9% Li_2ZrO_3 2.9% $LaAlO_3$	12.97	0.95±1.2	5.7±5.9	35

***Any wt.% below 2% was not reported as that is below the resolution of the instrument.**

Table 2: Summary of the electrochemical properties of LLZO-Al

Al-content (mol)	σ_{Total} (mS/cm)	σ_{Bulk} (mS/cm)	Grain Boundary Resistance (%)	Bulk Activation Energy (eV)	Grain Boundary Activation Energy (eV)
0.25	0.46±0.1	0.56±0.1	17.6±4.5	0.39±0.02	0.47±0.04
0.35	0.27±0.06	0.33±0.05	17.4±5.4	0.40±0.03	0.31±0.09
0.45	0.21±0.03	0.28±0.03	24.7±5.8	0.37±0.05	0.44±0.03
0.55	0.099±0.09	0.15±0.09	41.2±34.4	0.41±0.01	0.41±0.09

4. Conclusions

One method of achieving higher conductivity in LLZO is by doping it with aluminum to stabilize the cubic phase. However, little research has previously been done to simultaneously explore the effects of aluminum concentration on the microstructural and electrochemical properties of LLZO. To better understand the role of aluminum concentration on these properties, LLZO with nominal concentrations of 0.25, 0.35, 0.45, and 0.55 mol of aluminum were hot-pressed and analyzed using XRD, SEM, EBSD, EDS, TOF-SIMS, and EIS. It was found that the different aluminum concentrations do, indeed, play a significant role in the resulting microstructure and the electrochemical performance.

Through rapid induction hot-pressing, highly dense cubic LLZO samples were prepared. Our findings reveal that the solubility limit is approximately 0.40 mol of aluminum per formula unit of LLZO. Beyond the aluminum solubility limit secondary phases evolved at the grain boundaries of the LLZO. As the aluminum concentration increased further beyond the solubility limit, the concentration of secondary phases increased. Once a critical concentration was reached, these secondary phases contributed to the increases in grain boundary resistance. Furthermore, increases in aluminum concentration also led to decreases in bulk conductivity. The relatively constant bulk activation energies between the compositions studied suggest that the mobility term of the Nernst-Einstein equation was roughly independent of the aluminum concentration. Thus, the main variable controlling the decrease in bulk conductivity with the increase in aluminum concentration was the decrease in lithium charge carrier concentration. Based on the trends that grain boundary resistance increases and bulk conductivity decreases with increasing aluminum concentration, LLZO-Al0.25 exhibited the highest total conductivity of the tested compositions. While the activation energies of the grain boundaries of the other concentrations remained relatively constant, that of the LLZO-Al0.35 grain boundary was lower than that of the other compositions due to the extensive abnormal grain growth unique to this aluminum concentration. Apart from the secondary phase formation and abnormal grain growth, the microstructural features were similar across the compositions: they exhibited similar grain size, grain morphology, and grain boundary misorientation angles, as well as a lack of texturing. The electrochemical and microstructural observations provide a more comprehensive understanding of the effect of aluminum concentration on various properties of LLZO and how those properties, in turn, affect each other.

Based on our results, it is suggested that further work focus on higher resolution characterization of the grain boundaries via TEM and individual grain boundary electrochemistry to better understand the effect of the aluminum on the grain boundaries of LLZO. It is also suggested to further investigate the occupancy of the lithium and aluminum in the LLZO interstitials to elucidate the balance between structure, bulk conductivity, and activation energy. *In situ* sintering and densification observation at high resolution may also be helpful to determine the secondary phases present during sintering and whether liquid phase sintering may be occurring. Additionally, further investigation into the origins of abnormal grain growth in LLZO may prove fruitful in improving microstructural control through processing.

Author Contributions

Alexandra C. Moy – Formal analysis, Investigation, Visualization, Writing – original draft, Writing – review & editing
Grit Häuschen – Investigation, Validation
Dina Fattakhova-Rohlfing – Funding acquisition, Writing – review & editing

Jeffrey B. Wolfenstine – Writing – review & editing

Martin Finsterbusch – Conceptualization, Supervision, Visualization, Writing – original draft, Writing - review & editing

Jeff Sakamoto – Conceptualization, Funding acquisition, Supervision, Writing – review & editing

Conflicts of Interest

J.S. is the founder of Zakuro, Inc. that is developing garnet electrolyte technology. The other authors have no conflicts of interest to declare.

Acknowledgements

This work was part of the US-German joint collaboration on “Interfaces and Interphases in Rechargeable Li-Metal Based Batteries” supported by the US Department of Energy (DOE) and the German Federal Ministry of Education and Research (BMBF). Financial support from the BMBF under grant number 03XP0223E and DOE under the grant number DE-ACO5-000R22275 is acknowledged. The authors further would like to acknowledge the University of Michigan College of Engineering for financial support and the Michigan Center for Materials Characterization for use of the instruments and staff assistance. The authors would also like to acknowledge the use of ColorBrewer.org for colors used in Figures 9-11 and Figure S3. Additional support by the BMBF under grant number 13XP0173A (FestBatt-Oxide) and 13XP0434A (FB2-Oxide) as well as 13XP0258B (Meet Hi-EnD III) is gratefully acknowledged.

We would like to thank Dr. Sahir Naquash (IEK-1) and Dr. Uwe Breuer for the SIMS analysis and Dr. Volker Nischwitz for the ICP-OES Analysis (both from the Central Institute of Analytics – ZEA-3) at the Forschungszentrum Jülich.

5. References

1 A. Junio Samson, K. Hofstetter, S. Bag and V. Thangadurai, *Energy Environ. Sci.*, 2019, **12**, 2957–2975.

2 A. Manthiram, *ACS Cent. Sci.*, 2017, **3**, 1063–1069.

3 J. B. Goodenough and K.-S. Park, *J. Am. Chem. Soc.*, 2013, **135**, 1167–1176.

4 J. W. Choi and D. Aurbach, *Nat. Rev. Mater.*, 2016, **1**, 1–16.

5 X. Zeng, M. Li, D. Abd El-Hady, W. Alshitari, A. S. Al-Bogami, J. Lu and K. Amine, *Adv. Energy Mater.*, 2019, **9**, 1900161.

6 P. Albertus, S. Babinec, S. Litzelman and A. Newman, *Nat. Energy*, 2018, **3**, 16–21.

7 X.-B. Cheng, R. Zhang, C.-Z. Zhao and Q. Zhang, *Chem. Rev. (Washington, DC, U.S.)*, 2017, **117**, 10403–10473.

8 D. Lin, Y. Liu and Y. Cui, *Nat. Nanotechnol.*, 2017, **12**, 194–206.

9 X.-Q. Zhang, C.-Z. Zhao, J.-Q. Huang and Q. Zhang, *Engineering*, 2018, **4**, 831–847.

10 J.-M. Tarascon and M. Armand, *Nature*, 2001, **414**, 359–367.

11 B. Liu, J.-G. Zhang and W. Xu, *Joule*, 2018, **2**, 833–845.

12 J. Kasemchainan, S. Zekoll, D. Spencer Jolly, Z. Ning, G. O. Hartley, J. Marrow and P. G. Bruce, *Nat. Mater.*, 2019, **18**, 1105–1111.

13 B. Wu, S. Wang, J. Lochala, D. Desrochers, B. Liu, W. Zhang, J. Yang and J. Xiao, *Energy Environ. Sci.*, 2018, **11**, 1803–1810.

14 F. Han, J. Yue, X. Zhu and C. Wang, *Adv. Energy Mater.*, 2018, **8**, 1703644.

15 F. Han, A. S. Westover, J. Yue, X. Fan, F. Wang, M. Chi, D. N. Leonard, N. J. Dudney, H. Wang and C. Wang, *Nat. Energy*, 2019, **4**, 187–196.

16 T. Thompson, S. Yu, L. Williams, R. D. Schmidt, R. Garcia-Mendez, J. Wolfenstine, J. L. Allen, E. Kioupakis, D. J. Siegel and J. Sakamoto, *ACS Energy Lett.*, 2017, **2**, 462–468.

17 A. Luntz, *J. Phys. Chem. Lett.*, 2015, **6**, 300–301.

18 Y. Shimonishi, A. Toda, T. Zhang, A. Hirano, N. Imanishi, O. Yamamoto and Y. Takeda, *Solid State Ionics*, 2011, **183**, 48–53.

19 C. A. Geiger, E. Alekseev, B. Lazic, M. Fisch, T. Armbruster, R. Langner, M. Fechtelkord, N. Kim, T. Pettke and W. Weppner, *Inorg. Chem.*, 2011, **50**, 1089–1097.

20 I. Kokal, M. Somer, P. H. L. Notten and H. T. Hintzen, *Solid State Ionics*, 2011, **185**, 42–46.

21 E. Rangasamy, J. Wolfenstine and J. Sakamoto, *Solid State Ionics*, 2012, **206**, 28–32.

22 R. Murugan, V. Thangadurai and W. Weppner, *Angew. Chem. Int. Ed.*, 2007, **46**, 7778–7781.

23 H. Buschmann, J. Dölle, S. Berendts, A. Kuhn, P. Bottke, M. Wilkening, P. Heitjans, A. Senyshyn, H. Ehrenberg, A. Lotnyk, V. Duppel, L. Kienle and J. Janek, *Phys. Chem. Chem. Phys.*, 2011, **13**, 19378–19392.

24 S. Kumazaki, Y. Iriyama, K.-H. Kim, R. Murugan, K. Tanabe, K. Yamamoto, T. Hirayama and Z. Ogumi, *Electrochem. Commun.*, 2011, **13**, 509–512.

25 J. Awaka, N. Kijima, H. Hayakawa and J. Akimoto, *J. Solid State Chem.*, 2009, **182**, 2046–2052.

26 R. Murugan, S. Ramakumar and N. Janani, *Electrochem. Commun.*, 2011, **13**, 1373–1375.

27 Y. Li, C.-A. Wang, H. Xie, J. Cheng and J. B. Goodenough, *Electrochem. Commun.*, 2011, **13**, 1289–1292.

28 S. Ohta, T. Kobayashi and T. Asaoka, *J. Power Sources*, 2011, **196**, 3342–3345.

29 H. Buschmann, S. Berendts, B. Mogwitz and J. Janek, *J. Power Sources*, 2012, **206**, 236–244.

30 T. Thompson, J. Wolfenstine, J. L. Allen, M. Johannes, A. Huq, I. N. David and J. Sakamoto, *J. Mater. Chem. A*, 2014, **2**, 13431–13436.

31 J. Wolfenstine, J. Ratchford, E. Rangasamy, J. Sakamoto and J. L. Allen, *Mater. Chem. Phys.*, 2012, **134**, 571–575.

32 J. L. Allen, J. Wolfenstine, E. Rangasamy and J. Sakamoto, *J. Power Sources*, 2012, **206**, 315–319.

33 H. El Shinawi and J. Janek, *J. Power Sources*, 2013, **225**, 13–19.

34 D. Rettenwander, C. A. Geiger and G. Amthauer, *Inorg. Chem.*, 2013, **52**, 8005–8009.

35 L. Dhivya, N. Janani, B. Palanivel and R. Murugan, *AIP Adv.*, 2013, **3**, 082115.

36 Y. Jin and P. J. McGinn, *J. Power Sources*, 2011, **196**, 8683–8687.

37 A. Düvel, A. Kuhn, L. Robben, M. Wilkening and P. Heitjans, *J. Phys. Chem. C*, 2012, **116**, 15192–15202.

38 R. Sudo, Y. Nakata, K. Ishiguro, M. Matsui, A. Hirano, Y. Takeda, O. Yamamoto and N. Imanishi, *Solid State Ionics*, 2014, **262**, 151–154.

39 L. P. Cook, E. R. Plante, R. S. Roth and J. W. Hastie, US Department of Commerce, Phase Equilibria of Stored Chemical Energy Reactants, Gaithersburg, 1984.

40 N. C. Rosero-Navarro and K. Tadanaga, in *Solid Electrolytes for Advanced Applications: Garnets and Competitors*, eds. R. Murugan and W. Weppner, Springer Nature Switzerland AG, Cham, 1, 2019, 5, 111–128.

41 L. Cheng, J. Sun Park, H. Hou, V. Zorba, G. Chen, T. Richardson, J. Cabana, R. Russo and M. Doeff, *J. Mater. Chem. A*, 2014, **2**, 172–181.

42 B. Gao, R. Jalem and Y. Tateyama, *J. Mater. Chem. A*, 2022, DOI:10.1039/D2TA00545J.

43 J. Wolfenstine, J. Sakamoto and J. L. Allen, *J. Mater. Sci.*, 2012, **47**, 4428–4431.

44 S. Mukhopadhyay, T. Thompson, J. Sakamoto, A. Huq, J. Wolfenstine, J. L. Allen, N. Bernstein, D. A. Stewart and M. D. Johannes, *Chem. Mater.*, 2015, **27**, 3658–3665.

45 D. Rettenwander, P. Blaha, R. Laskowski, K. Schwarz, P. Bottke, M. Wilkening, C. A. Geiger and G. Amthauer, *Chem. Mater.*, 2014, **26**, 2617–2623.

46 S. Smetaczek, A. Wachter-Welzl, R. Wagner, D. Rettenwander, G. Amthauer, L. Andrejs, S. Taibl, A. Limbeck and J. Fleig, *J. Mater. Chem. A*, 2019, **7**, 6818–6831.

47 M. Mann, M. Küpers, G. Häuschen, M. Finsterbusch, D. Fattakhova-Rohlfing and O. Guillon, *Materials*, 2021, **14**, 6809.

48 Y. Arinicheva, X. Guo, M.-T. Gerhards, F. Tietz, D. Fattakhova-Rohlfing, M. Finsterbusch, A. Navrotsky and O. Guillon, *Chem. Mater.*, 2022, **34**, 1473–1480.

49 T. F. Malkowski, E. D. Boeding, D. Fattakhova-Rohlfing, N. Wettengl, M. Finsterbusch and G. M. Veith, *Ionics*, 2022, DOI:10.1007/s11581-022-04536-0.

50 K. Iltgen, C. Bendel, A. Benninghoven and E. Niehuis, *J. Vac. Sci. Technol. A*, 1997, **15**, 460–464.

51 C. Dellen, H.-G. Gehrke, S. Möller, C.-L. Tsai, U. Breuer, S. Uhlenbruck, O. Guillon, M. Finsterbusch and M. Bram, *J. Power Sources*, 2016, **321**, 241–247.

52 R. A. Huggins, *Ionics*, 2002, **8**, 300–313.

53 M. Huang, T. Liu, Y. Deng, H. Geng, Y. Shen, Y. Lin and C.-W. Nan, *Solid State Ionics*, 2011, **204–205**, 41–45.

54 A. A. Hubaud, D. J. Schroeder, B. Key, B. J. Ingram, F. Dogan and J. T. Vaughey, *J. Mater. Chem. A*, 2013, **1**, 8813–8818.

55 J. Wolfenstine, J. L. Allen, J. Sakamoto, D. J. Siegel and H. Choe, *Ionics*, 2018, **24**, 1271–1276.

56 A. Sharafi, C. G. Haslam, R. D. Kerns, J. Wolfenstine and J. Sakamoto, *J. Mater. Chem. A*, 2017, **5**, 21491–21504.

57 W. D. Kingery, H. K. Bowen and D. R. Uhlmann, *Introduction to Ceramics*, John Wiley & Sons, New York, 2, 1976.

58 L. Cheng, C. H. Wu, A. Jarry, W. Chen, Y. Ye, J. Zhu, R. Kostecki, K. Persson, J. Guo, M. Salmeron, G. Chen and M. Doeff, *ACS Appl. Mater. Interfaces*, 2015, **7**, 17649–17655.

59 L. Cheng, E. J. Crumlin, W. Chen, R. Qiao, H. Hou, S. F. Lux, V. Zorba, R. Russo, R. Kostecki, Z. Liu, K. Persson, W. Yang, J. Cabana, T. Richardson, G. Chen and M. Doeff, *Phys. Chem. Chem. Phys.*, 2014, **16**, 18294–18300.

60 G. Larraz, A. Orera and M. L. Sanjuán, *J. Mater. Chem. A*, 2013, **1**, 11419–11428.

61 I. N. David, T. Thompson, J. Wolfenstine, J. L. Allen and J. Sakamoto, *Journal of the American Ceramic Society*, 2015, **98**, 1209–1214.

62 P. Wu and A. D. Pelton, *J. Alloys Compd.*, 1992, **179**, 259–287.

63 E. E. Hellstrom and W. Van Gool, *Solid State Ionics*, 1981, **2**, 59–64.

64 K.-Y. Yang, K.-Z. Fung and I.-C. Leu, *J. Alloys Compd.*, 2007, **438**, 207–216.

65 M. Wang, J. B. Wolfenstine and J. Sakamoto, *Electrochim. Acta*, 2019, **296**, 842–847.

66 W. E. Tenhaeff, E. Rangasamy, Y. Wang, A. P. Sokolov, J. Wolfenstine, J. Sakamoto and N. J. Dudney, *ChemElectroChem*, 2014, **1**, 375–378.

67 J. B. Goodenough, presented as a review lecture, Inorganic Chemistry Laboratory, South Parks Road, Oxford, OX1 3QR, UK, June, 1982.